



Repositorio Institucional de la Universidad Autónoma de Madrid

<https://repositorio.uam.es>

Esta es la **versión de autor** del artículo publicado en:

This is an **author produced version** of a paper published in:

The Journal of Physical Chemistry C 124.4 (2020): 2619-2626

DOI: <https://doi.org/10.1021/acs.jpcc.9b11084>

Copyright: © 2020 American Chemical Society

El acceso a la versión del editor puede requerir la suscripción del recurso

Access to the published version may require subscription

Mixed-Valence Lanthanide-Activated Phosphors: Invariance of the Intervalence Charge Transfer (IVCT) Absorption Onset Across the Series.

Ivo Neefjes,[†] Jonas J. Joos,[‡] Zoila Barandiarán,[¶] and Luis Seijo*,[¶]

[†]*Department of Chemistry, KU Leuven, Celestijnenlaan 200F, B-3001 Leuven, Belgium*

[‡]*LumiLab, Department of Solid State Sciences, and Center for Nano- and Biophotonics (NB-Photonics), Ghent University, B-9000 Ghent, Belgium*

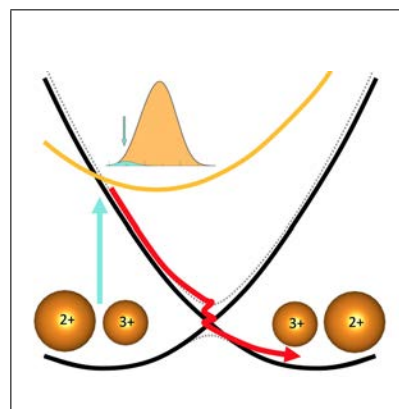
[¶]*Departamento de Química, Instituto Universitario de Ciencia de Materiales Nicolás Cabrera, and Condensed Matter Physics Center (IFIMAC), Universidad Autónoma de Madrid, 28049 Madrid, Spain*

E-mail: luis.seijo@uam.es

Abstract

Recently, direct evidence was given for the existence of intervalence charge transfer (IVCT) states of $\text{Eu}^{2+}/\text{Eu}^{3+}$ pairs in Eu-doped fluorite hosts and their signature in absorption spectra was characterized [J. Phys. Chem. Lett. 10(2019)1851]. Here we show, by means of multiconfigurational *ab initio* calculations, that the IVCT absorptions of all $2+/3+$ mixed valence lanthanides doped in CaF_2 start basically at the same energy. This is rationalized with a simplified model of IVCT absorptions. Emissions above that energy are expected to be partly or totally quenched when $2+/3+$ pairs are formed. On the basis of this finding and existing calculations, we report expected IVCT absorptions of mixed valence lanthanides doped in several fluoride, oxide, and sulfide hosts.

Graphical TOC Entry



Keywords

Intervalence charge transfer, IVCT, Europium, Eu, CaF_2 , fluorite, luminescence quenching

Introduction

According to IUPAC recommendations, intervalence charge transfer (IVCT) is the name given to an electron transfer between two metal sites differing only in oxidation state, $M^{n+}-M^{(n+1)+} \rightarrow M^{(n+1)+}-M^{n+}$,^{1,2} even though it is sometimes used for electron transfer between different metals. IVCT states have an important potential to impact the luminescence of lanthanide activated inorganic phosphors by quenching and excitation loss. Yet, they are very elusive for direct experimental measurements and not much is known about them (their absorption bands are extremely broad and flat, their intensity is low, and no emission follows the IVCT absorptions).³ This is why we dedicate this paper to studying the energies of IVCT states of mixed valence lanthanide ions doped in crystalline solids. We focus on the onsets of optical IVCT absorptions across the lanthanide series, which we study by means of state-of-the-art multiconfigurational *ab initio* calculations. We discuss next the antecedents.

Whereas the literature on IVCT between transition metal ions is abundant,⁴⁻⁶ the number of studies on IVCT between lanthanide ions is very scarce. Among the latter, the majority focus on thermally induced electron transfer in mixed valence compounds, the pioneering work of Berkooz *et al.*⁷ in the mixed valence Europium sulfide Eu_3S_4 being a good example. However, very few pay attention to photoinduced electron transfer, which should provide the information on the IVCT state energies and their potential impact on luminescence. The reports by Wickleder on $\text{Eu}^{2+}/\text{Eu}^{3+}$ IVCT absorption bands in the mixed valence Europium chlorides $\text{Na}_5\text{Eu}_7\text{Cl}_{22}$ and KEu_2Cl_6 ^{8,9} are an exception to this.

In lanthanide-doped crystalline materials the number of studies on IVCT states has been very limited. This is so in spite of the fact that these lanthanide-activated materials play a crucial role as inorganic phosphors with many technological applications, ranging from light-emitting diodes, scintillators or radiation dosimeters,¹⁰⁻¹³ to glow-in-the-dark road marks, thermometry or infrared-phosphor-

based in-vivo medical imaging or theranostics.¹⁴⁻¹⁶ As a matter of fact, for decades, only the tentative assignment of a broad band in the reflection spectrum of Ce-doped LaPO_4 as a $\text{Ce}^{3+}/\text{Ce}^{4+}$ IVCT absorption by van Schaik *et al.*¹⁷ could be cited. Recently, the importance of these materials as phosphors and the suspicion that the presence of mixed valence dopant pairs or clusters might have an important impact on their luminescence, boosted new research on the role of electron transfer between two oxidation states of the optically active dopants. E.g., the anomalous emissions of Ce-doped elpasolites and Yb-doped fluorides, and the laser-induced white emission from Ce in Sr_2CeO_4 , have been interpreted as IVCT luminescences with the assistance of multiconfigurational *ab initio* calculations.¹⁸⁻²⁰ Direct experimental proof of the IVCT nature of excited states is still a big challenge, but recent experiments showed evidence that the anomalous emission of $\text{CaF}_2:\text{Yb}^{2+}$ is not due to impurity-trapped-excitons,²¹ which was the accepted model during three decades. They also demonstrated the true $\text{Yb}^{2+}/\text{Yb}^{3+}$ mixed valence nature of Ytterbium in $\text{CaF}_2:\text{Yb}^{2+}$ and its inherent complexity,²² so moving the focus towards the importance of IVCT states.

In spite of the elusiveness of the IVCT states, direct evidence of IVCT absorptions of $\text{Eu}^{2+}/\text{Eu}^{3+}$ pairs in Eu-doped CaF_2 , SrF_2 , and BaF_2 was recently provided in a combined experimental and *ab initio* study.³ The compatibility of the IVCT states with Eu^{2+} $d-f$ luminescence in CaF_2 and SrF_2 was shown to turn into IVCT-driven $d-f$ luminescence quenching in BaF_2 ,³ which was a clear example of the potential impact of IVCT states in phosphors.

Here, we report multiconfigurational *ab initio* calculations of the IVCT absorptions of $\text{Ln}^{2+}/\text{Ln}^{3+}$ pairs in Ln-doped CaF_2 for the entire lanthanide series (Ln=Ce, Pr, Nd, Pm, Sm, Eu, Gd, Tb, Dy, Ho, Er, Tm, Yb). They are useful, e.g., for understanding the potential role of divalent/trivalent lanthanide ions when present -on purpose or unintentionally- in hosts activated with the trivalent/divalent counterparts. This is interesting because, although only a few divalent doped lanthanide

ions are stable in regular conditions, most of them have been stabilized under suitable treatments, like x-ray and gamma irradiation^{23–25} and, as a matter of fact, the entire series of rare earths can exist in the divalent state when present in small amounts in crystalline CaF_2 .²³

We show that the computed IVCT states of all $\text{Ln}^{2+}/\text{Ln}^{3+}$ lanthanide pairs in CaF_2 start at basically the same energy. This finding is compatible with a simple model of IVCT states,²⁶ according to which, for given ligands and coordination number, the maximum of the absorption to the first IVCT state (i.e. the onset of the full IVCT absorption band) depends only on two simple structural properties of the electron donor and acceptor active centers: the difference between their lanthanide-ligand bond lengths, $d(\text{Ln}^{2+}\text{-L}) - d(\text{Ln}^{3+}\text{-L})$, and the average of their breathing mode vibrational frequencies. Based on this result, we report predicted IVCT absorptions of lanthanide ions in a few other hosts where *ab initio* calculations of these properties are available.

The paper opens the door to predicting IVCT states onsets of any lanthanide mixed valence pair in a host with relatively simple structural calculations of two oxidation states of a single lanthanide element in the host. Other alternatives for the prediction of the onsets are experimental measurements (on one lanthanide element only) of vibrational frequencies and bond length differences or their empirical estimates (e.g. using ionic radii for the latter²⁶).

Theoretical methods

We computed the diabatic potential energy surfaces for electron transfer states of $\text{Ln}^{2+}/\text{Ln}^{3+}$ mixed valence pairs in CaF_2 ($\text{Ln}=\text{Ce}, \text{Pr}, \text{Nd}, \text{Pm}, \text{Sm}, \text{Eu}, \text{Gd}, \text{Tb}, \text{Dy}, \text{Ho}, \text{Er}, \text{Tm}, \text{Yb}$), and the corresponding IVCT configuration coordinate energy level diagrams, using the results of independent embedded cluster calculations as proposed in Refs. 18 and 19.

We assumed the lanthanide ions substitute for Ca^{2+} in CaF_2 and we calculated the electronic structures of the electron donor and acceptor octahedral embedded clusters $(\text{LnF}_8)^{6-}$

Table 1: Lowest free-ion and O_h terms.

Ln^{2+}	Ln^{3+}	Config.	Free-ion term	O_h terms
	Ce^{3+}	$4f^1$	$^2F^o$	$^2A_{2u}, ^2T_{1u}, ^2T_{2u}$
Ce^{2+}	Pr^{3+}	$4f^2$	3H	$^3E_g, 2\ ^3T_{1g}, ^3T_{2g}$
Pr^{2+}	Nd^{3+}	$4f^3$	$^4I^o$	$^4A_{1u}, ^4A_{2u}, ^4E_u, ^4T_{1u}, 2\ ^4T_{2u}$
Nd^{2+}	Pm^{3+}	$4f^4$	5I	$^5A_{1g}, ^5A_{2g}, ^5E_g, ^5T_{1g}, 2\ ^5T_{2g}$
Pm^{2+}	Sm^{3+}	$4f^5$	$^6H^o$	$^6E_u, 2\ ^6T_{1u}, ^6T_{2u}$
Sm^{2+}	Eu^{3+}	$4f^6$	7F	$^7A_{2g}, ^7T_{1g}, ^7T_{2g}$
Eu^{2+}	Gd^{3+}	$4f^7$	$^8S^o$	$^8A_{1u}$
Gd^{2+}	Tb^{3+}	$4f^8$	7F	$^7A_{2g}, ^7T_{1g}, ^7T_{2g}$
Tb^{2+}	Dy^{3+}	$4f^9$	$^6H^o$	$^6E_u, 2\ ^6T_{1u}, ^6T_{2u}$
Dy^{2+}	Ho^{3+}	$4f^{10}$	5I	$^5A_{1g}, ^5A_{2g}, ^5E_g, ^5T_{1g}, 2\ ^5T_{2g}$
Ho^{2+}	Er^{3+}	$4f^{11}$	$^4I^o$	$^4A_{1u}, ^4A_{2u}, ^4E_u, ^4T_{1u}, 2\ ^4T_{2u}$
Er^{2+}	Tm^{3+}	$4f^{12}$	3H	$^3E_g, 2\ ^3T_{1g}, ^3T_{2g}$
Tm^{2+}	Yb^{3+}	$4f^{13}$	$^2F^o$	$^2A_{2u}, ^2T_{1u}, ^2T_{2u}$
Yb^{2+}		$4f^{14}$	1S	$^1A_{1g}$

and $(\text{LnF}_8)^{5-}$. We also assumed a non-local long-range charge compensation for Ln^{3+} . We performed the calculations with the suite of programs MOLCAS,²⁷ using D_{2h} symmetry, in two step spin-orbit coupling SA-CASSCF/MS-CASPT2/RASSI-SO DKH calculations that are described next: In a first step, we used the spin-orbit-free many-electron relativistic second-order Douglas-Kroll-Hess (DKH) Hamiltonian^{28,29} and performed all-electron calculations with the same type of basis set used in the calculations of $\text{CaF}_2:\text{Yb}^{2+}, \text{Yb}^{3+}$ in Ref. 19: Gaussian atomic natural orbital relativistic basis sets ANO-RCC for the lanthanides³⁰ and Fluorine,³¹ with respective contractions $(25s22p15d11f4g2h)/[9s8p5d4f3g2h]$ (quadruple-zeta with polarization quality) and $(14s9p4d)/[5s4p3d]$ (quadruple-zeta with polarization without f -functions quality); plus the occupied $3s$ and $3p$ orbitals of the embedding Ca^{2+} ions, contracted as $(20s15p)/[1s1p]$ and located at the 12 neighbour sites $(\frac{1}{2}, \frac{1}{2}, 0)$, which act as cluster-host orthogonalization functions;³² and 5 s -type Gaussian type functions located at the six $(\frac{1}{2}, 0, 0)$ interstitial sites surrounding the LnF_8 cube in the fluorite structure, whose orbital exponents were optimized to give minimal impurity-trapped exciton energy in $\text{CaF}_2:\text{Yb}^{2+}$.¹⁹ In this step, we performed state-average restricted-active-space self-consistent-field (SA-CASSCF)^{33–35} calculations allowing all possible occupations in the $\text{Ln } 4f$ shells and up to 4 electrons in

the Ln $5f$ shells, in order to account for the so-called double-shell effect, whose importance when dealing with orbital shells of different occupancies was originally shown in transition metal ions^{36,37} and more recently confirmed in lanthanide ions.³⁸ In these SA-CASSCF calculations, we averaged all states of equal spin and spatial irreducible representation that result from the ligand-field splitting of the lowest free-ion lanthanide ion terms; they are listed in Table 1. Subsequent multi-state second-order perturbation theory (MS-CASPT2)^{39–42} calculations allowed to correlate all cluster valence electrons, except the $4d$ electrons of the lanthanides. We used a standard IPEA value (0.25 au)⁴³ and an imaginary shift of 0.15 au.⁴⁴

In the second step, we added the AMFI approximation of the DKH spin-orbit coupling (SOC) operator to the Hamiltonian⁴⁵ and we performed restricted-active-space state-interaction spin-orbit (RASSI-SO)^{46,47} calculations where all states of a given cluster computed in the first step were allowed to interact.

In these calculations, the clusters were embedded in *ab initio* model potentials (AIMP)⁴⁸ that include Coulomb, exchange, and Pauli repulsion interactions from the CaF_2 host lattice obtained in Ref. 19 from self-consistent embedded-ions (SCEI)⁴⁹ Hartree-Fock calculations (Ref. 27).

Results

Before we discuss the results, let us make some theoretical considerations on the onsets of the IVCT absorption bands we calculate here.

The first consideration is that the spin-orbit coupling (SOC) interactions between spin-orbit-free states considered in this work (cf. Table 1) would in some cases be insufficient for an accurate description of a number of lowest spin-orbit states. E.g. in Pr^{3+} , SOC interactions between the 3H and 3F related states are known to be necessary.⁵⁰ However, the considered SOC interactions are sufficient for the accuracies of spin-orbit ground state energies, bond lengths, and vibrational frequencies demanded for a reliable calculation of the IVCT absorptions on-

sets, which are on focus here. We illustrate this with calculations of the IVCT configuration coordinate diagram and absorption band of $\text{Sm}^{2+}/\text{Sm}^{3+}$ pairs in CaF_2 , which are shown in Fig. 1.

In the left panel of Fig. 1 we show the IVCT configuration coordinate diagram as computed in this work, i.e. with SOC interactions between the 7F related states of Sm^{2+} , on one hand, and the 6H related states of Sm^{3+} , on the other. The band profile corresponding to the first individual IVCT absorption (indicated with a vertical blue arrow on the left panel) was calculated with the parabolas of the ground state and the first IVCT state using the time-dependent approach of Heller;^{51,52} it is shown in blue in the upper right panel. This individual IVCT absorption is a very broad band. And the same is true for all other individual IVCT absorption bands. The reason for this is the very large horizontal offset between the minima of the parabolas of the Sm^{2+} - Sm^{3+} and Sm^{3+} - Sm^{2+} configurations of the pair.¹⁸ This large offset is in turn a consequence of the strong relaxations that take place around the two ions of the pair after the electron transfer: after the electron leaves Sm^{2+} , this becomes Sm^{3+} and the ligands get much closer to it; simultaneously, after the electron reaches Sm^{3+} , this becomes Sm^{2+} and the ligands expand a lot around it. This band maximum is calculated at 14150 cm^{-1} . Now, when the calculation is improved and SOC interactions between the 6H and 6F related states of Sm^{3+} are included, we get the IVCT configuration coordinate diagram of the center panel of Fig. 1. The band maximum of the first individual IVCT absorption remains practically unchanged: 14210 cm^{-1} .

A second consideration is how the maximum of the first individual IVCT absorption is rendered in experimental spectra. For this, we recall that real IVCT absorption bands result from the convolution of many individual IVCT absorptions, due to the crowdedness of Ln^{3+} and Ln^{2+} states right above the ground state,³ which makes them broader than the individual ones. In the case of $\text{Sm}^{2+}/\text{Sm}^{3+}$ pairs in CaF_2 , the convolution of all the individual absorptions in the center panel of Fig. 1 is shown in orange

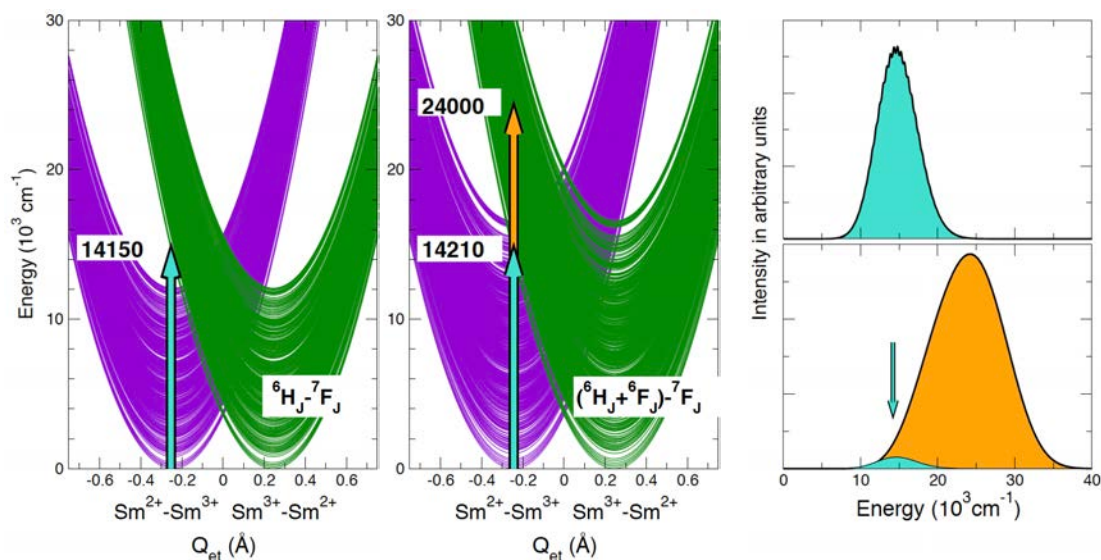


Figure 1: Left and center: IVCT energy diagrams of $\text{Sm}^{2+}/\text{Sm}^{3+}$ mixed valence pairs in CaF_2 . $\text{Sm}^{2+}(4f^6 {}^7F_J)/\text{Sm}^{3+}(4f^5 {}^6H_J)$ IVCT states (left) and $\text{Sm}^{2+}(4f^6 {}^7F_J)/\text{Sm}^{3+}(4f^5 {}^6H_J, {}^6F_J)$ IVCT states (center). Right: first individual IVCT absorption band as calculated with the left diagram (above) and convoluted, full IVCT absorption band as calculated with the center diagram (below). The blue arrow in the right panel indicates the position of the former in the latter and illustrates how the maximum of the first individual absorption band marks the onset of the full IVCT absorptions. The orange arrow in the center panel indicates the energy of the full IVCT absorption maximum.

in the bottom right panel, where the contribution of the first individual IVCT absorption is shown in blue. It is clear that the maximum of the first individual IVCT absorption as calculated in this paper (upper right panel) perfectly marks the onset of the full IVCT absorption (lower right panel), as it would be obtained experimentally.

A final consideration concerns the role of states of the $4f^{N-1}5d^1$ configuration of some divalent lanthanides, which also induce more IVCT states and hence absorptions. When their energy is higher than the $4f^N$ ground state, even if they are almost degenerate, they alter the shape of the full IVCT absorption, but not its onset. When their energy is lower and the ground configuration is $4f^{N-1}5d^1$ (this is e.g. the case of Gd^{2+} in CaF_2 ²³), the $4f^N$ IVCT configuration coordinate diagrams calculated here do not represent the true IVCT absorptions. However, we expect the conclusions extracted here for $4f \rightarrow 4f$ IVCT absorption onsets also to hold in these cases, because, as we will see below, the IVCT absorption onsets are determined by the bond lengths and vibrational frequencies, and these are not very different in

$4f^N$ and $4f^{N-1}5d^1$ states.^{53,54}

Let us now discuss the results. In Fig. 2, we show the calculated IVCT configuration coordinate energy level diagrams of the $\text{Ln}^{2+}/\text{Ln}^{3+}$ pairs in CaF_2 for the entire lanthanide series. In Table 2 (second column), we show the computed IVCT absorption onset of each rare earth pair (i.e. the maximum of the first individual IVCT absorption), which is also indicated in the Figure.

One can see in Fig. 2 and Tab. 2 that the $4f \rightarrow 4f$ IVCT absorption onset is basically constant across the series. The differences between rare earths are hardly significant having in mind the very broad nature of these absorptions. This invariance is the most remarkable feature of the results and we discuss it next.

According to the Frank-Condon rule, the maximum of the first individual IVCT absorption occurs at the energy necessary to go from $\text{Ln}^{2+}\text{-Ln}^{3+}$ at its equilibrium (initial state of the absorption) to $\text{Ln}^{3+}\text{-Ln}^{2+}$ (final state of the absorption) at fixed positions of the nuclei, i.e. without changing the atomistic structure. This energy difference is represented with vertical blue arrows in the configuration coordinate en-

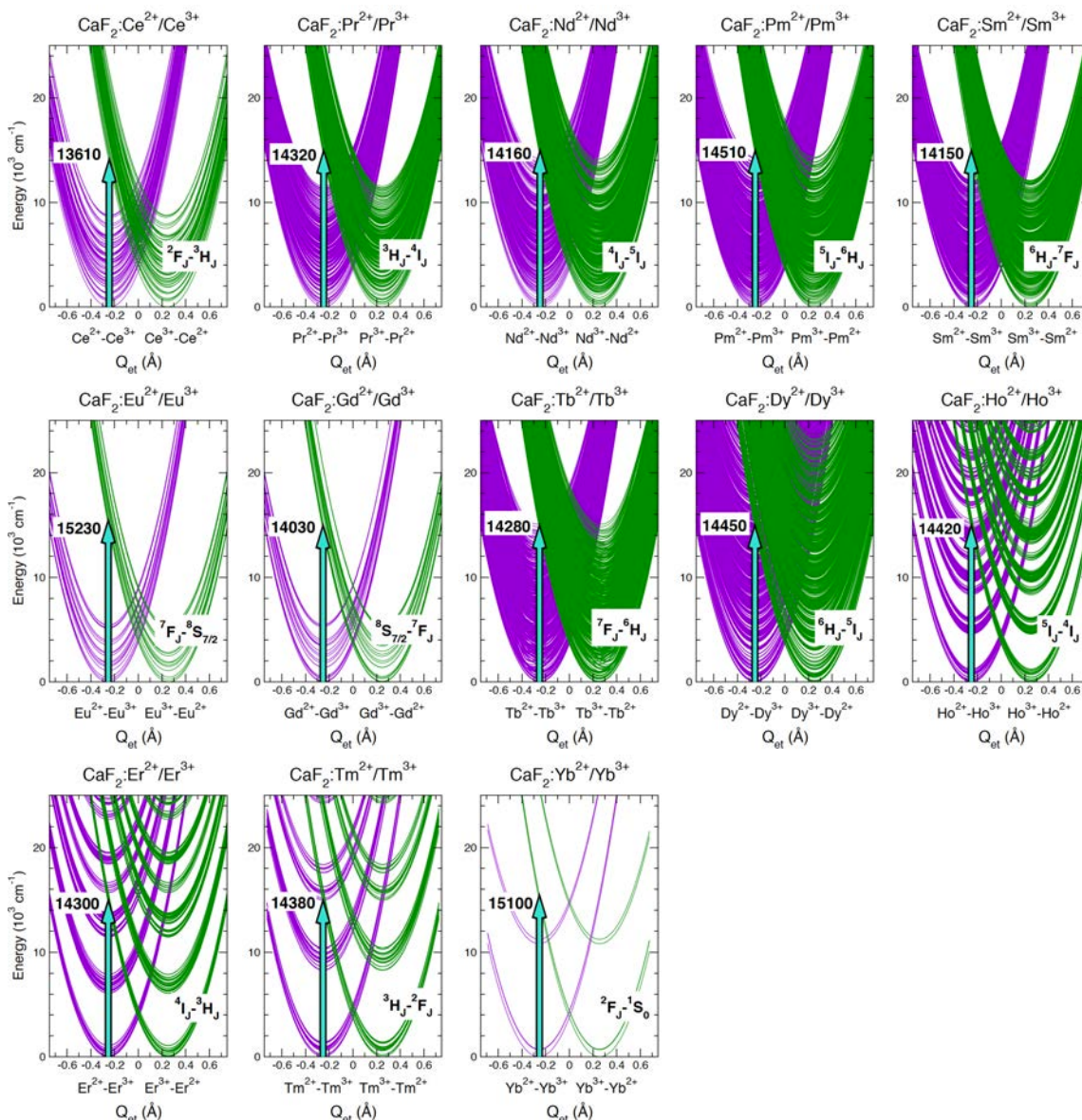


Figure 2: IVCT energy diagrams of $\text{Ln}^{2+}/\text{Ln}^{3+}$ mixed valence pairs in CaF_2 . Only $\text{Ln}^{2+}(4f^{N+1})/\text{Ln}^{3+}(4f^N)$ levels are shown. The onset of the $\text{Ln}^{2+}4f \rightarrow \text{Ln}^{3+}4f$ IVCT absorption (understood as the maximum of the lowest individual IVCT absorption band) is indicated with a turquoise vertical arrow.

ergy diagrams of Fig. 2.

This photoinduced electron transfer is followed by no emission. Instead, a non-radiative decay with a strong structural reorganization takes place in which the ligands experience a large compression around Ln^{3+} and a large expansion around Ln^{2+} . Since $\text{Ln}^{2+}-\text{Ln}^{3+}$ and $\text{Ln}^{3+}-\text{Ln}^{2+}$ have the same energies at their respective equilibrium structures, the IVCT absorption energy coincides with the structural reorganization energy, which depends entirely on structural parameters. This energy is, according to the simple predictive model of IVCT

states of Ref. 26:

$$E_{\text{IVCT}}^{\text{abs}} = 2kQ_{\text{et},0}^2, \quad (1)$$

where k is an effective breathing mode force constant of donor and acceptor centers, in $\text{cm}^{-1}/\text{\AA}^2$, and $Q_{\text{et},0}$ is the electron transfer reaction coordinate, or configuration coordinate, at equilibrium, in \AA . They read, respectively,

$$k = 0.02966 \mu \bar{\nu}_{\text{ave}}^2, \quad (2)$$

where μ is the ligand mass (in amu) and $\bar{\nu}_{\text{ave}}$ is the average of the breathing mode vibrational

Table 2: Computed maxima of the first $\text{Ln}^{2+}/\text{Ln}^{3+}$ IVCT absorptions (in cm^{-1}), electron donor and acceptor bond lengths ($d(\text{Ln}-\text{F})$, in Å), and breathing mode vibrational frequencies ($\bar{\nu}_{a_{1g}}$, in cm^{-1}) of $\text{CaF}_2:\text{Ln}^{2+}, \text{Ln}^{3+}$. Results of the absorption predicted with the IVCT model out of Donor-Acceptor bond length differences ($\Delta d_{DA} = d(\text{Ln}^{2+}-\text{F}) - d(\text{Ln}^{3+}-\text{F})$, in Å) and average vibrational frequencies ($\bar{\nu}_{ave}$, in cm^{-1}) are also given.

	$\text{Ln}^{2+}/\text{Ln}^{3+}$ IVCT absorption onset	Ln^{2+} donor		Ln^{3+} acceptor		Δd_{DA}		IVCT model (Ref. 26)	
		$d_{\text{Ln}-\text{F}}$	$\bar{\nu}_{a_{1g}}$	$d_{\text{Ln}-\text{F}}$	$\bar{\nu}_{a_{1g}}$		$\bar{\nu}_{ave}$	IVCT absorption onset (Eq. 4)	diff.
Ce	13610	2.432	420	2.311	494	0.121	457	13790	180
Pr	14320	2.422	426	2.300	495	0.122	461	14230	-90
Nd	14160	2.412	427	2.289	495	0.123	461	14500	340
Pm	14510	2.401	426	2.278	495	0.123	461	14460	-50
Sm	14150	2.387	422	2.266	498	0.121	460	13970	-180
Eu	15230	2.387	421	2.260	495	0.127	458	15250	20
Gd	14030	2.375	423	2.252	494	0.123	459	14340	310
Tb	14280	2.368	422	2.244	494	0.124	458	14540	260
Dy	14450	2.360	420	2.235	492	0.125	456	14650	200
Ho	14420	2.352	420	2.226	495	0.126	458	14980	560
Er	14300	2.345	419	2.219	491	0.126	455	14820	520
Tm	14380	2.337	417	2.212	491	0.125	454	14520	140
Yb	15100	2.329	421	2.200	491	0.129	456	15600	500

frequencies of donor and acceptor centers (in cm^{-1}), and

$$Q_{et,0} = \sqrt{\frac{n}{2}} \Delta d_{DA}, \quad (3)$$

where n is the coordination number of donor and acceptor, and Δd_{DA} (in Å) is the difference between the lanthanide-ligand distances in the donor and acceptor centers, $\Delta d_{DA} = d(\text{Ln}^{2+}-\text{L}) - d(\text{Ln}^{3+}-\text{L})$.

Eq. 1 can be rewritten in terms of n , μ , $\bar{\nu}_{ave}$ and Δd_{DA} as

$$E_{\text{IVCT}}^{\text{abs}} = 0.02966 \cdot n \cdot \mu \cdot \bar{\nu}_{ave}^2 \cdot (\Delta d_{DA})^2. \quad (4)$$

We include in Table 2 the *ab initio* results for these structural data together with the IVCT absorption energy calculated with Eq. 4.

It is clear that the simple model correctly reproduces the *ab initio* IVCT absorptions and their invariance across the series. Furthermore, the reliability of the model allows one to state that the reason for the invariance of the *ab initio* IVCT absorptions is the invariance of both $\bar{\nu}_{ave}$ and Δd_{DA} across the series. The rather

constant value of the vibrational frequency (and its corresponding force constant) is a manifestation of the very weak involvement of the unfilled $4f$ shell in a bond dominated by the rare earths' $5s, 5p$ filled shells. The almost invariant value of Δd_{DA} is the result of the lanthanide contraction being similar in the divalent and trivalent ions.

One should expect all these arguments to hold for other hosts and other pairs of oxidation states like $\text{Ln}^{3+}/\text{Ln}^{4+}$, in which case the conclusion that the IVCT absorption onset in a host is basically constant across the series would be a general conclusion. In other words, knowing (from experiments or calculations) the IVCT absorption onset of a pair of oxidations states of one rare earth in a host is sufficient to know the same property of the other rare earths in the same host.

According to this, we show in Table 3 the values of IVCT absorption energies of the lanthanides in a few hosts, as predicted by *ab initio* calculations. The results in CaS, SrS, and BaS have been calculated for this work, the others are taken from literature. These data are

Table 3: *Ab initio* IVCT absorption onsets (in cm^{-1}) of mixed valence lanthanides doped in crystalline hosts.

Host	Mixed valence	IVCT absorption onset	Calculated Ln	Reference
CaF ₂	Ln ²⁺ /Ln ³⁺	14500	all	This work, 3,19
SrF ₂	Ln ²⁺ /Ln ³⁺	18000	Eu,Yb	3,19
BaF ₂	Ln ²⁺ /Ln ³⁺	22500	Eu,Yb	3,19
SrCl ₂	Ln ²⁺ /Ln ³⁺	8100	Yb	19
CaS	Ln ²⁺ /Ln ³⁺	10400	Eu	This work
SrS	Ln ²⁺ /Ln ³⁺	12800	Eu	This work
BaS	Ln ²⁺ /Ln ³⁺	18100	Eu	This work
SrS	Ln ³⁺ /Ln ⁴⁺	10000	Ce	55 (empirical)
Cs ₂ LiLuCl ₆	Ln ³⁺ /Ln ⁴⁺	10000	Ce	18
CaTiO ₃	Ln ³⁺ /Ln ⁴⁺	12000	Pr	56
CaZrO ₃	Ln ³⁺ /Ln ⁴⁺	12800	Pr	56

graphically represented in Fig. 3 as a function of breathing mode force constant k and electron transfer reaction coordinate at equilibrium $Q_{et,0}$, which can straightforwardly be obtained from Eqs. 2 and 3 using ligand masses, breathing mode vibrational frequencies, coordination numbers, and Ln-L bond length differences between donor and acceptor. The color map in the background of the figure represents the IVCT absorption onset E_{IVCT}^{abs} according to Eq. 1.

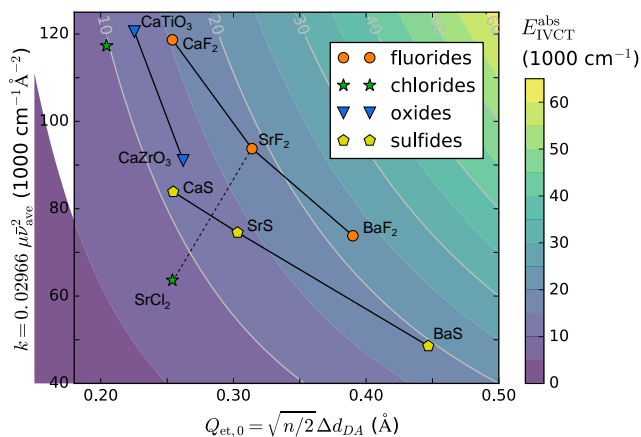


Figure 3: Calculated IVCT absorption onset E_{IVCT}^{abs} as a function of the two parameters $Q_{et,0}$ and k (electron transfer reaction coordinate at equilibrium and breathing mode force constant) according to Eq. 1 for a selection of host compounds. The color map and light gray isolines display the value of E_{IVCT}^{abs} . Straight lines connect isostructural hosts differing only in one cation (solid lines) or one anion (dashed line).

From this two-parameter model (Eq. 1)²⁶ a systematic host dependence of the IVCT absorption onsets emerges that deserves further *ab initio* study. The available data at this point indicates, nevertheless, that cation substitution,

a strategy often used to fine-tune the properties of luminescent materials, impacts E_{IVCT}^{abs} via both parameters of the model. The change in bond length upon charge transfer, Δd_{DA} , increases appreciably when going from a host with a small cation site towards one with a larger cation site, resulting in a shift to the right in the diagram of Fig. 3. Simultaneously, the vibrational frequency $\bar{\nu}_{\text{ave}}$ decreases following the bond length elongations, resulting in a downshift in Fig. 3. Both effects are visualized by solid black lines in Fig. 3 for the isostructural fluorides (MF₂, M=Ca,Sr,Ba), sulfides (MS, M=Ca,Sr,Ba) and perovskites (CaAO₃, A=Ti,Zr).

Another possibility to alter the vibrational frequency is upon replacement of the anions in the compound, i.e. the ligands of the lanthanide ion. The force constant k , to which E_{IVCT}^{abs} is directly proportional, is affected because the nature of the chemical bond as well as the ligand mass will change. As an example, the dashed line in Fig. 3 illustrates the effect when moving from SrF₂ to the isostructural SrCl₂. This shows that replacing the anion has a roughly orthogonal effect to changing the cation in the two-dimensional parameter space. The effect on Δd_{DA} and k upon changing the ligand of the lanthanide ion results in a systematic redshift in E_{IVCT}^{abs} according to the sequence $F > O \geq S > Cl$. This sequence, emerging from the computed data and the model given by Eqs. 1-4 offers a semi-quantitative tool to predict the location of IVCT states for mixed valence lanthanide pairs, Ln²⁺/Ln³⁺ or Ln³⁺/Ln⁴⁺ in a variety of host compounds.

Since IVCT states can cause luminescence quenching and even complete luminescence excitation loss,³ according to the present IVCT diagrams (cf. Fig. 2), it is suggested that the IVCT absorption onsets reported are in fact emission energy thresholds, i.e., all emissions of higher energies than they are expected to be partly or totally quenched by the presence of the respective mixed valence pairs. E.g., the presence of Ln²⁺/Ln³⁺ mixed valence pairs in CaF₂ is expected to partly or totally quench all emissions of an energy higher than 14000 cm^{-1} . In some cases, like Tb and Dy, the crowded-

ness of states suggests that all emissions well above that threshold will be quenched. In other cases, like Tm and Yb, the discontinuity of states creates energy windows where metastable states and their emissions can exist, although the mixed valence pairs are expected to partly quench them, leading to a worsened thermal quenching behavior and a lowered photoluminescence quantum efficiency. Finding these metastable states above the first IVCT absorption energies demands careful analysis case by case.

Conclusions

Multiconfigurational *ab initio* calculations on divalent/trivalent mixed-valence lanthanide ions doped in CaF₂ show that the IVCT absorption onset is basically invariant across the lanthanide series in a given host. The onset sets an energy threshold for partial or total luminescence quenching when mixed-valence pairs are formed in the lanthanide-doped host.

The invariance of the IVCT absorption onset is rationalized by using a simple model of IVCT absorptions.²⁶ According to it, the IVCT invariance is a consequence of respective invariances of the breathing mode vibrational frequency, on one hand, and the difference between lanthanide-ligand bond lengths in the two oxidation states, $d(\text{Ln}^{2+}\text{-L}) - d(\text{Ln}^{3+}\text{-L})$, on the other. The latter is, in turn, a consequence of the lanthanide contractions of divalent and trivalent ions being very similar. The model points out systematic host dependences of the lanthanide IVCT absorption onsets.

Acknowledgement This work was partially supported by Ministerio de Economía y Competitividad, Spain (Dirección General de Investigación y Gestión del Plan Nacional de I+D+i, MAT2017-83553-P).

References

- (1) Verhoeven, J. W. Glossary of Terms Used in Photochemistry (IUPAC Recommendations 1996). *Pure Appl. Chem.* **1996**, *68*, 2223–2286.
- (2) Nic, M.; Jirat, J.; Kosata, B. IUPAC Gold Book. <https://doi.org/10.1351/goldbook.I03125>, 2006-; Accessed: 2019-06-10.
- (3) Joos, J.; Seijo, L.; Barandiarán, Z. Direct Evidence of Intervalence Charge-Transfer States of Eu-Doped Luminescent Materials. *J. Phys. Chem. Lett.* **2019**, *10*, 1581–1586.
- (4) Marcus, R. A. Chemical and Electrochemical Electron-Transfer Theory. *Annu. Rev. Phys. Chem.* **1964**, *15*, 155–196.
- (5) Allen, G. C.; Hush, N. S. Intervalence-Transfer Absorption. Part 1. Qualitative Evidence for Intervalence-Transfer Absorption in Inorganic Systems in Solution and in the Solid State. *Prog. Inorg. Chem.* **1967**, *8*, 357–389.
- (6) Robin, M.; Day, P. Mixed Valence Chemistry - A Survey and Classification. *Adv. Inorg. Chem. Radiochem.* **1968**, *10*, 247–422.
- (7) Berkooz, O.; Malamud, M.; Shtrikman, S. Observation of Electron Hopping in ¹⁵¹Eu₃Eu₄ by Mössbauer Spectroscopy. *ssc* **1968**, *6*, 185–188.
- (8) Wickleder, C. A New Mixed Valent Europium Chloride: Na₅Eu₇Cl₂₂. *Z. Naturforsch.* **2002**, *57b*, 901–907.
- (9) Wickleder, C. KEu₂Cl₆ and K_{1.6}Eu_{1.4}Cl₅: Two New Mixed-Valent Europium Chlorides. *Z. Anorg. Allg. Chem.* **2002**, *628*, 1815–1820.
- (10) Shulg'in, B. V.; Buzmakova, S. I.; Viktorov, L. V.; Krymov, A. L.; Petrov, V. L.; Podurovskii, S. V.; Kozlov, A. A.; Shapiro, B. M.; Shrom, M. Y.; Nepomnyashchikh, A. I. et al. Scintillation Detectors Working with CaF₂-Eu Single-Crystals. *Atom. Energy* **1993**, *75*, 534–538.

- (11) Leblans, P.; Vandenbroucke, D.; Willems, P. Storage Phosphors for Medical Imaging. *Materials* **2011**, *4*, 1034–1086.
- (12) Smet, P. F.; Parmentier, A. B.; Poelman, D. Selecting Conversion Phosphors for White Light-Emitting Diodes. *J. Electrochem. Soc.* **2011**, *158*, R37–R54.
- (13) Abé, S.; Joos, J. J.; Martin, L. I. D. J.; Hens, Z.; Smet, P. F. Hybrid Remote Quantum Dot/Powder Phosphor Designs for Display Backlights. *Light: Sci. Appl.* **2017**, *6*, e16271.
- (14) Maldiney, T.; Bessiere, A.; Seguin, J.; Teston, E.; Sharma, S. K.; Viana, B.; Bos, A. J. J.; Dorenbos, P.; Bessodes, M.; Gourier, D. et al. The In Vivo Activation of Persistent Nanophosphors for Optical Imaging of Vascularization, Tumours and Grafted Cells. *Nature Materials* **2014**, *13*, 418–426.
- (15) Botterman, J.; Smet, P. F. Persistent Phosphor $\text{SrAl}_2\text{O}_4\text{:Eu,Dy}$ in Outdoor Conditions: Saved by the Trap Distribution. *Opt. Express* **2015**, *23*, A868–A881.
- (16) Xu, J.; Tanabe, S. Persistent Luminescence Instead of Phosphorescence: History, Mechanism, and Perspective. *J. Lumin.* **2019**, *205*, 581–620.
- (17) van Schaik, W.; Lizzo, S.; Smit, W.; Blasse, G. Influence of Impurities on the Luminescence Quantum Efficiency of $(\text{La,Ce,Tb})\text{PO}_4$. *J. Electrochem. Soc.* **1993**, *140*, 216–222.
- (18) Seijo, L.; Barandiarán, Z. Intervalence Charge Transfer Luminescence: The Anomalous Luminescence of Ce-Doped $\text{Cs}_2\text{LiLuCl}_6$ Elpasolite. *J. Chem. Phys.* **2014**, *141*, 214706/1–214706/14.
- (19) Barandiarán, Z.; Seijo, L. Intervalence Charge Transfer Luminescence: Interplay Between Anomalous and $5d - 4f$ Emissions in Yb-Doped Fluorite-Type Crystals. *J. Chem. Phys.* **2014**, *141*, 234704.
- (20) Streck, W.; Tomala, R.; Marciniak, L.; Lukaszewicz, M.; Cichy, B.; Stefanski, M.; Hreniak, D.; Kedzierski, A.; Krosnicki, M.; Seijo, L. Broadband anti-Stokes white emission of Sr_2CeO_4 nanocrystals induced by laser irradiation. *Phys. Chem. Chem. Phys.* **2016**, *18*, 27921–27927.
- (21) MacKeen, C.; Bridges, F.; Kozina, M.; Mehta, A.; Reid, M. F.; Wells, J.-P. R.; Barandiarán, Z. Evidence That the Anomalous Emission from $\text{CaF}_2\text{:Yb}^{2+}$ Is Not Described by the Impurity Trapped Exciton Model. *J. Phys. Chem. Lett.* **2017**, *8*, 3313–3316.
- (22) MacKeen, C.; Bridges, F.; Seijo, L.; Barandiarán, Z.; Kozina, M.; Mehta, A.; Reid, M. F.; Wells, J.-P. R. The Complexity of the $\text{CaF}_2\text{:Yb}$ System: A Huge, Reversible, X-ray-Induced Valence Reduction. *J. Phys. Chem. C* **2017**, *121*, 28435–28442.
- (23) McClure, D. S.; Kiss, Z. Survey of the Spectra of the Divalent Rare-Earth Ions in Cubic Crystals. *J. Chem. Phys.* **1963**, *39*, 3251.
- (24) Merz, J. L.; Pershan, P. S. Charge Conversion of Irradiated Rare-Earth Ions in Calcium Fluoride. I. *Phys. Rev.* **1967**, *162*, 217–235.
- (25) Merz, J. L.; Pershan, P. S. Charge Conversion of Irradiated Rare-Earth Ions in Calcium Fluoride. II. Thermoluminescent Spectra. *Phys. Rev.* **1967**, *162*, 235–247.
- (26) Barandiarán, Z.; Meijerink, A.; Seijo, L. Configuration Coordinate Energy Level Diagrams of Intervalence and Metal-to-Metal Charge Transfer States of Dopant Pairs in Solids. *Phys. Chem. Chem. Phys.* **2015**, *17*, 19874–19884.
- (27) Karlström, G.; Lindh, R.; Malmqvist, P. A.; Roos, B. O.; Ryde, U.; Veryazov, V.; Widmark, P. O.; Cossi, M.; Schimmelpfennig, B.; Neogrady, P. et al.

- MOLCAS: A Program Package for Computational Chemistry. *Comput. Mater. Sci.* **2003**, *28*, 222–239.
- (28) Douglas, M.; Kroll, N. M. Quantum Electrodynamical Corrections to the Fine Structure of Helium. *Ann. Phys. (N.Y.)* **1974**, *82*, 89–155.
- (29) Hess, B. A. Relativistic Electronic-Structure Calculations Employing a Two-Component No-Pair Formalism with External-Field Projection Operators. *Phys. Rev. A* **1986**, *33*, 3742–3748.
- (30) B. O. Roos, R. Lindh, P. A. Malmqvist, V. Veryazov, P. O. Widmark,; Borin, A. C. New Relativistic Atomic Natural Orbital Basis Sets for Lanthanide Atoms with Applications to the Ce Diatom and LuF₃. *J. Phys. Chem. A* **2008**, *112*, 11431–11435.
- (31) Roos, B. O.; Lindh, R.; Malmqvist, P. A.; Veryazov, V.; Widmark, P. O. Main Group Atoms and Dimers Studied with a New Relativistic ANO Basis Set. *J. Phys. Chem. A* **2004**, *108*, 2851–2858.
- (32) Pascual, J. L.; Seijo, L.; Barandiarán, Z. Ab initio model potential study of environmental effects on the Jahn-Teller parameters of Cu²⁺ and Ag²⁺ impurities in MgO, CaO and SrO hosts. *J. Chem. Phys.* **1993**, *98*, 9715.
- (33) Roos, B. O.; Taylor, P. R.; Siegbahn, P. E. M. A Complete Active Space SCF Method (CASSCF) Using a Density-Matrix Formulated Super-CI Approach. *Chem. Phys.* **1980**, *48*, 157–173.
- (34) Siegbahn, P. E. M.; Heiberg, A.; Roos, B. O.; Levy, B. Comparison of the Super-CI and the Newton-Raphson Scheme in the Complete Active Space SCF Method. *Phys. Scr.* **1980**, *21*, 323–327.
- (35) Siegbahn, P. E. M.; Heiberg, A.; Almlöf, J.; Roos, B. O. The Complete Active Space SCF (CASSCF) Method in a Newton-Raphson Formulation with Application to the HNO Molecule. *J. Chem. Phys.* **1981**, *74*, 2384–2396.
- (36) Froese-Fischer, C. Oscillator Strengths for ²S – ²P Transitions in the Copper Sequence. *J. Phys. B* **1977**, *10*, 1241.
- (37) T. H. Dunning, Jr., B. H. Botch,; J. F. Harrison, On the orbital description of the 4s3d(n+1) states of the transition metal atoms. *J. Chem. Phys.* **1980**, *72*, 3419.
- (38) Barandiarán, Z.; Seijo, L. Radial correlation effects on interconfigurational excitations at the end of the lanthanide series: A restricted active space second order perturbation study of Yb²⁺ and SrCl₂:Yb²⁺. *J. Chem. Phys.* **2013**, *138*, 074102.
- (39) Andersson, K.; Malmqvist, P.-A.; Roos, B. O.; Sadlej, A. J.; Wolinski, K. Second-Order Perturbation Theory with a CASSCF Reference Function. *J. Phys. Chem.* **1990**, *94*, 5483–5488.
- (40) Andersson, K.; Malmqvist, P.-A.; Roos, B. O. Second-Order Perturbation Theory with a Complete Active Space Self-Consistent Field Reference Function. *J. Chem. Phys.* **1992**, *96*, 1218–1226.
- (41) Zaitsevskii, A.; Malrieu, J.-P. Multi-Partitioning Quasidegenerate Perturbation Theory. A New Approach to Multireference Møller-Plesset Perturbation Theory. *Chem. Phys. Lett.* **1995**, *233*, 597–604.
- (42) Finley, J.; Malmqvist, P.-A.; Roos, B. O.; Serrano-Andrés, L. The Multi-State CASPT2 Method. *Chem. Phys. Lett.* **1998**, *288*, 299–306.
- (43) G. Ghigo, B. O. Roos,; P.-Å. Malmqvist, A modified definition of the zeroth-order Hamiltonian in multiconfigurational perturbation theory (CASPT2). *Chem. Phys. Lett.* **2004**, *396*, 142.

- (44) Forsberg, N.; Malmqvist, P.-A. Multi-configuration Perturbation Theory with Imaginary Level Shift. *Chem. Phys. Lett.* **1997**, *274*, 196.
- (45) Hess, B. A.; Marian, C. M.; Wahlgren, U.; Gropen, O. A Mean-Field Spin-Orbit Method Applicable to Correlated Wavefunctions. *Chem. Phys. Lett.* **1996**, *251*, 365–371.
- (46) Malmqvist, P. A.; Roos, B. O.; Schimelpfennig, B. The RASSI Approach with Spin-Orbit Coupling. *Chem. Phys. Lett.* **2002**, *357*, 230–240.
- (47) Paulovic, J.; Nakajima, T.; Hirao, K.; Lindh, R.; Malmqvist, P.-A. Relativistic and Correlated Calculations on the Ground and Excited States of ThO. *J. Chem. Phys.* **2003**, *119*, 798–805.
- (48) Barandiarán, Z.; Seijo, L. The Ab Initio Model Potential Representation of the Crystalline Environment. Theoretical Study of the Local Distortion on NaCl:Cu⁺. *J. Chem. Phys.* **1988**, *89*, 5739–5746.
- (49) Seijo, L.; Barandiarán, Z. Ab Initio Model Potential Study of Local Distortions Around Cr⁺ and Cr³⁺. *J. Chem. Phys.* **1991**, *94*, 8158.
- (50) Krośnicki, M.; K? D? Ydzierski, A.; Seijo, L.; Barandiarán, Z. Ab Initio Theoretical Study on the 4f² and 4f5d Electronic Manifolds of Cubic Defects in CaF₂:Pr³⁺. *J. Phys. Chem. A* **2014**, *118*, 358–68.
- (51) Heller, E. J. Time-Dependent Approach to Semiclassical Dynamics. *J. Chem. Phys.* **1975**, *62*, 1544.
- (52) Heller, E. J. The Semiclassical Way to Molecular Spectroscopy. *Acc. Chem. Res.* **1981**, *14*, 368.
- (53) Barandiarán, Z.; Seijo, L. In *Computational Methods in Lanthanide and Actinide Chemistry*; Dolg, M., Ed.; John Wiley & Sons: New York, 2015; pp 217–240.
- (54) de Jong, M.; Meijerink, A.; Seijo, L.; Barandiarán, Z. Energy Level Structure and Multiple 4f¹²5d¹ Emission Bands of Tm²⁺ in Halide Perovskites: Theory and Experiment. *J. Phys. Chem. C* **2017**, *121*, 10095–10101.
- (55) Kulesza, D.; Cybińska, J.; Seijo, L.; Barandiarán, Z.; Zych, E. Anomalous Red and Infrared Luminescence of Ce³⁺ Ions in SrS:Ce Sintered Ceramics. *J. Phys. Chem. C* **2015**, *119*, 27649–27656.
- (56) Barandiarán, Z.; Bettinelli, M.; Seijo, L. Color Control of Pr³⁺ Luminescence by Electron-Hole Recombination Energy Transfer in CaTiO₃ and CaZrO₃. *J. Phys. Chem. Lett.* **2017**, *8*, 3095–3100.